

Electronic charge redistribution in $\text{LaAlO}_3(001)$ thin films deposited at $\text{SrTiO}_3(001)$ substrate: First principles analysis and the role of stoichiometry

Alexandre Sorokin,^{1,2,*} Dmitry Bocharov,^{1,3} Sergei Piskunov,^{2,3} and Vyacheslavs Kashcheyevs^{1,3}

¹*Faculty of Physics and Mathematics, University of Latvia, 8 Zellu Str., Riga LV-1002, Latvia*

²*Institute for Solid State Physics, University of Latvia, 8 Kengaraga Str., Riga LV-1063, Latvia*

³*Faculty of Computing, University of Latvia, 19 Raina blvd., Riga LV-1586, Latvia*

We present a comprehensive first-principles study of the electronic charge redistribution in atomically sharp $\text{LaAlO}_3/\text{SrTiO}_3(001)$ heterointerfaces of both n- and p-types allowing for non-stoichiometric composition. Using two different computational methods within the framework of the density functional theory (linear combination of atomic orbitals and plane waves) we demonstrate that conducting properties of $\text{LaAlO}_3/\text{SrTiO}_3(001)$ heterointerfaces strongly depend on termination of $\text{LaAlO}_3(001)$ surface. We argue that both the polar “catastrophe” and the polar distortion scenarios may be realized depending on the interface stoichiometry. Our calculations predict that heterointerfaces with a non-stoichiometric film—either LaO-terminated n-type or AlO_2 -terminated p-type—may exhibit the conductivity of n- or p-type, respectively, independently of $\text{LaAlO}_3(001)$ film thickness.

PACS numbers: 68.35.Ct, 68.35.Md, 73.20.At

I. INTRODUCTION

The discovery of conducting interface between two initially insulating materials— TiO_2 -terminated (001) surface of SrTiO_3 (STO) substrate and LaAlO_3 (LAO) thin film deposited atop of it¹—has attracted strong scientific interest during the last few years.^{2–5} The high application potential of LAO/STO heterointerfaces has been demonstrated, e.g., by fabrication of highly voltage-tunable oxide diode⁶ that utilizes the advantage of the electric-field controlled interfacial metal-insulator transition of LAO/STO.^{7,8}

Several competing mechanisms for the origin of the charge carriers responsible for conductivity and the structure of the LAO/STO conducting layer have been suggested. The first one is the “polar catastrophe” model⁹ which considers intrinsic electronic reconstruction due to the polar discontinuity at the atomically sharp interface. Assuming the electrostatics of formal ion charges, layer by layer growth of LAO on STO in [001] direction leads to a growing electrical potential due to accumulation of alternating dipoles through the LAO film. Due to multivalent nature of the $\text{Ti}^{3+/4+}$ cations, the electronic reconstruction is possible by transferring half an electron to the Ti cation in case of $\text{La}^{3+}\text{O}^{2-}/\text{Ti}^{4+}\text{O}_2^{2-}$ n-type (n-LAO/STO) interface, or by transferring half a hole to the $\text{Al}^{3+}\text{O}_2^{2-}/\text{Sr}^{2+}\text{O}^{2-}$ p-type (p-LAO/STO) interface, to remove the internal polarization and prevent the “catastrophe”. This charge transfer would result in a doped interface layer which may explain the observed conductivity.⁹ Since this model is based on atomically sharp interfaces its relevance depends on experimental feasibility of fabrication of nearly atomically sharp interfaces. Such possibility is provided by molecular beam epitaxy (MBE) in which the thermal energies of evaporated incident ions are on the order of 0.1 eV, i.e., much lower than the kinetic energy (~ 10 eV) of the incident ions in pulsed laser deposition (PLD), thus MBE avoids in-

termixing of cations at the interface.^{5,10} Transport measurements performed on conducting n-LAO/STO with LAO film thickness above 4 unit cells (UC’s) reveal sheet carrier density n_s of $\sim 1\text{--}3 \times 10^{13} \text{ cm}^{-2}$ after annealing,¹⁰ which is in good agreement with theoretical predictions given for atomically sharp n-LAO/STO:^{11–13} an abrupt insulating-to-metallic transition occurs at LAO film thickness above 5 UC with $n_s \approx 2 - 7 \times 10^{13} \text{ cm}^{-2}$. p-LAO/STO interfaces have shown no measurable conductivity independently of LAO film thickness.¹⁰

The second proposed mechanism is a formation of high density of oxygen vacancies, which are generated in the STO substrate during the deposition of LAO thin film and can be responsible for increase of sheet carrier density up to $5 \times 10^{17} \text{ cm}^{-2}$ for PLD-grown n-LAO/STO interface if the sample is not annealed.^{1,14} The insulating behavior of p-LAO/STO has been also ascribed to that the holes can be trapped by the two electrons located at the oxygen vacancies created in the STO substrate.¹⁵

The third scenario for LAO/STO interface conductivity is based on the suggestion that the La/Sr cation intermixing due to ion bombardment effect (inherent in PLD and post-growth treatment) may lead to the formation of one or two layers of metallic $\text{La}_{1-x}\text{Sr}_x\text{TiO}_3$.^{5,16,17} The thermodynamical stability for intermixed configurations has been recently reported.^{5,18}

We believe that any of the mechanisms mentioned may be consistent with the corresponding set of experimental results, however, the whole picture for adequate interpretation of experimental observations in line with theoretical predictions is not yet fully clear. One of the reasons is that most of the first principles studies describing structural and electronic properties of LAO/STO interfaces assume that the LAO films are perfectly stoichiometric. However, both in PLD and MBE experimental techniques used to produce atomically sharp interfaces, the vaporization process used to facilitate transfer through the vapor LAO phase is not guaranteed to preserve the

target stoichiometry.⁵ Recent report indicate that La/Al ratio of nonstoichiometric LAO films may be controlled during its epitaxial growth.^{19,20}

In this theoretical study we contrast stoichiometric and non-stoichiometric structures and argue that stoichiometry is a major factor that determines the build-up of charge responsible for conductivity in atomically sharp interfaces. We perform systematic first principles investigation of both stoichiometric and non-stoichiometric interfaces with up to eleven alternating $(\text{LaO})^+$ and $(\text{AlO}_2)^-$ monolayers of LAO deposited monolayer-by-monolayer atop an atomically flat STO(001) substrate. Our calculations show that *stoichiometric* interfaces tolerate the “polar catastrophe”⁹: It is energetically more favorable for them to keep the internal electric field that distorts the band edges and may eventually lead to conductivity if the film thickness is sufficient. This part of our work fully supports the polar distortion mechanism proposed by Pentcheva *et al.*⁴ for stoichiometric interfaces. Using the same methods, we find that the *non-stoichiometric* structures show an opposite tendency: There is a significant charge transfer to the surface layers which compensates the electrostatic field in the depth of the structure. This charge accumulation may be sufficient to cause the surface layers to conduct, in line with “polar catastrophe” scenario.⁹ Thus, the electronic structure of a LAO/STO(001) interface may be dictated by either the “polar catastrophe” or the polar distortion mechanism depending on the stoichiometry. As the substrates in the structures of either stoichiometry are equivalent, it is mainly the LAO film that determines the properties of the whole interface.

We have employed the methods of *ab initio* calculations based on the density functional theory (DFT) using hybrid exchange–correlation computational scheme to study the fully relaxed structures of LAO/STO interfaces under consideration. The B3PW functional,²¹ used in the CRYSTAL code²² with atomic basis set (BS), contains a “hybrid” of the DFT exchange and correlation functionals with exact non-local Hartree–Fock (HF) exchange. For comparison, the selected set of interface configurations have been also modeled using the Perdew–Wang generalized gradient approximation (PW91-GGA) density functional^{23,24} as implemented in the periodic plane-wave (PW) code VASP.²⁵

The outline of the paper is as follows. Section II describes the computational details of our calculations. The main part of the paper is formed by Sec. III. In Sec. III A we give an estimate of the thermodynamic stability and discuss the electronic structure of ideal LaO- and AlO_2 -terminated LAO(001) surfaces. Section III B presents atomic structure and electronic charge distribution for a range of n-LAO/STO and p-LAO/STO heterointerfaces and discusses their relation to the experimental and computational data available in the literature. Our conclusions are summarized in Section IV.

II. COMPUTATIONAL METHODS

In this study LAO/STO heterointerfaces are modeled by means of two different methods: (i) linear combination of atomic orbitals (LCAO) within the framework of hybrid density functional approach, and (ii) PW calculations using the GGA density functional.

To perform hybrid LCAO calculations, we used the periodic CRYSTAL code,²² which employs Gaussian-type functions centered on atomic nuclei as the BSs for expansion of the crystalline orbitals. The BSs used in this study were taken from the following sources: For Sr, Ti and O in the form of 311d1G, 411d311dG, and 8-411d1G, respectively, from Ref.26; for Al in the form of 8-621d1G from Ref.27; for La in the form of 311-31d3f1 from CRYSTAL’s homepage²² (*f*-type polarization Gaussian function with the exponent $\alpha = 0.475$ has been added according to prescription given in Ref.28). For Al and O all electrons are explicitly included. The inner core electrons of Sr and Ti are described by small-core Hay–Wadt effective pseudopotentials,²⁹ while the nonrelativistic pseudopotential of Dolg *et al.*³⁰ was adopted for La.

We employ the hybrid B3PW exchange–correlation functional²¹ which accurately reproduces the basic bulk and surface properties of a number of ABO_3 perovskite materials.^{26,31–33} The cutoff threshold parameters of CRYSTAL for Coulomb and exchange integrals evaluation (ITOL1–ITOL5) have been set to 7, 8, 7, 7, and 14, respectively. Calculations were considered as converged only when the total energy obtained in the self-consistency procedure differed by less than 10^{-7} a.u. in two successive cycles. Effective charges on atoms as well as net bond populations have been calculated according to the Mulliken population analysis.²²

As the second method the periodic total-energy code VASP²⁵ based on the use of a PW BS was applied. The cut-off energy has been chosen to be 520 eV. The non-local GGA exchange–correlation functional Perdew–Wang-91 (PW91) was employed.^{23,24} Scalar relativistic projector augmented wave (PAW) pseudopotentials in our calculations contain 11 valence electrons ($5s^25p^65d^16s^2$) for La, 3 electrons ($3s^23p^1$) for Al, 10 electrons ($4s^24p^65s^2$) for Sr, 12 electrons ($3s^23p^63d^24s^2$) for Ti, and 6 electrons ($2s^22p^4$) for O, respectively. Bader topological analysis³⁴ has been adopted to obtain net charges on atoms in VASP calculations.

In both VASP and CRYSTAL calculations the reciprocal space integration was performed by sampling the Brillouin zone with the $8 \times 8 \times 1$ Pack–Monkhorst mesh³⁵ for all surface structures under consideration. For bulk computations we applied sampling with the $8 \times 8 \times 8$ Pack–Monkhorst mesh. Such samplings provide balanced summation in direct and reciprocal lattices.

Taking into account that STO substrate at room temperature possesses perfect cubic structure, in our study we treat both LAO and STO in their high symmetry $Pm\bar{3}m$ cubic phase. Table I lists main bulk properties for both crystals. We note that the band gaps obtained by

TABLE I: Calculated equilibrium lattice constants (a_0 in Å), atomic net charges (Q_{atom} in e), cation–O bond populations ($P_{\text{A/B–O}}$ in milli e), and band gaps (δ in eV) of bulk LAO and STO in their high-symmetry $Pm\bar{3}m$ cubic phase. Shown are data obtained by means of both hybrid B3PW and standard GGA PW91 functionals. Negative bond population means atomic repulsion. Last two columns contain available experimental results for comparison.

	LAO (B3PW)	LAO (PW91)	STO (B3PW)	STO (PW91)	LAO (Exp.)	STO (Exp.)
a_0	3.802	3.808	3.910	3.918	3.811 ³⁶	3.905 ³⁷
$Q_{\text{La/Sr}}$	2.43	2.14	1.87	1.60	–	–
$Q_{\text{Al/Ti}}$	2.07	3.00	2.35	2.10	–	–
Q_{O}	–1.50	–1.78	–1.41	–1.23	–	–
$P_{\text{La/Sr–O}}$	4	–	–10	–	–	–
$P_{\text{Al/Ti–O}}$	152	–	88	–	–	–
δ	5.51	3.18	3.64	1.77	5.6 ³⁸	3.25 ³⁹

means of hybrid B3PW computation scheme are in better agreement with experimentally observed results. Therefore in this paper we mainly discuss the results obtained by means of B3PW while results obtained using PW91 functional are published for comparative purposes in order to make our study consistent with earlier *ab initio* calculations performed basically on LDA- or GGA-DFT ground.

Surface structures were modeled using a single slab model for LCAO calculations and a multi-slab model with vacuum gap of 20 Å for PW calculation. To compensate the dipole moment arises at charged surfaces, our slabs are symmetrically terminated. STO substrate contains 11 alternating (SrO)⁰ and (TiO_2)⁰ atomic monolayers, while from 1 to 11 alternating (LaO)⁺ and (AlO_2)[–] atomic monolayers were used for LAO film of the LAO/STO interface. Coordinates of all atoms in the LAO/STO heterointerfaces were allowed to relax. Due to symmetry constrains atomic displacements were allowed only along z -axis. Taking into account that the mismatch of $\sim 2.5\%$ between LAO and STO lattice constants arises during LAO epitaxial growth, in our modeling we have allowed relaxation of their joint lattice constant to minimize the strain effect. Computing Δz displacement for each monolayer of LAO/STO we took into account the shift of the preceding atomic monolayer. The reference z -coordinate for each monolayer N is defined as follows:

$$z_N^{\text{ref}} = \frac{1}{2} (z_{N-1}^{\text{Me}} + z_{N-1}^{\text{O}}), \quad (1)$$

where z_{N-1}^{Me} and z_{N-1}^{O} are z -coordinates of the cation and the anion of a preceding atomic monolayer, respectively.

TABLE II: Surface rumpling (s in Å) and changes in interplane distances (Δd_{ij} in Å, i and j are surface monolayers' numbers) of the three near-surface monolayers for the LaO- and AlO_2 -terminated LAO(001) surfaces as calculated by means of hybrid B3PW exchange–correlation functional.

	s	Δd_{12}	Δd_{23}
LaO-term.	0.314	–0.142	0.076
AlO_2 -term.	0.058	–0.052	0.045

III. RESULTS AND DISCUSSION

A. LAO(001) surfaces

Before general discussion of LAO/STO interfaces studied here, in this subsection we provide a comprehensive description of electronic and thermodynamic properties of both LaO- and AlO_2 -terminated pristine LAO(001) thin films.

1. Atomic and electronic properties

Pristine LAO(001) thin films were modeled using symmetrical 9-monolayer slab model. Considering formal ionic charges, LAO(001) has alternating (LaO)⁺ and (AlO_2)[–] surface monolayers and can be either LaO- or AlO_2 -terminated surface. Both LaO- and AlO_2 -terminations are studied. La/Al excess ratio is 1.25 and 0.8 for LaO- and AlO_2 -terminated LAO(001) films, respectively. Monolayers in LAO(001) possess a net charge, the repeat slab unit cell has a non-zero dipole moment and therefore LAO(001) is type III polar surface according to Tasker's classification.⁴⁰ This means, that perfect and unreconstructed (1×1) LAO(001) surfaces considered here can be stabilized by transferring of a half an electron (or hole) from the surface to the slab body that normally results in atomic and electronic reconfiguration at the surface.

Due to symmetry restrictions, atoms in LAO(001) surface slabs of both terminations were relaxed along z -axis only. Table II lists the structural parameters of the relaxed surfaces. The surface rumpling s denotes the relative displacement of oxygen with respect to the metal atom in the surface layer, while Δd_{12} and Δd_{23} (1, 2, and 3 are the numbers of near-surface monolayers) are the changes in interplane distances, where each monolayer is defined by the position of a cation. In good qualitative agreement with earlier first-principle calculations performed on pristine LAO(001)^{41–44} our calculations predict the amplitude of surface rumpling of LaO-terminated LAO(001) much larger than that of AlO_2 -terminated surface. The change in interplane distances Δd_{12} are also much better pronounced for LaO-terminated surface, while Δd_{23} are quite modest for both terminations meaning that significant surface relaxation

TABLE III: Calculated deviations in surface monolayer net charge (ΔQ in e), and deviations of cation–O bond populations ($\Delta P_{A/B-O}$ in milli e) in corresponding atomic monolayer relative to the bulk values (see Table I). Shown are data obtained by means of hybrid B3PW exchange–correlation functional. Surface monolayers are numbered beginning from the center of the slab (0 means the central monolayer of the symmetrical slab unit cell).

No.	M-layer	LaO-term.		M-layer	AlO ₂ -term.	
		ΔQ	$\Delta P_{A/B-O}$		ΔQ	$\Delta P_{A/B-O}$
4	LaO	−0.32	10	AlO ₂	0.46	100
3	AlO ₂	−0.02	−16	LaO	−0.02	−4
2	LaO	−0.09	0	AlO ₂	0.02	−10
1	AlO ₂	0.00	−2	LaO	−0.02	−4
0	LaO	−0.05	−2	AlO ₂	0.02	−10

does not go deeper than 2–3 surface monolayers.

In Table III we list the changes in surface (LaO)⁺ and (AlO₂)[−] monolayer net charges with respect to their bulk values (see Table I). Due to partly covalent nature of La–O and Al–O bonds (positive $P_{A/B-O}$ in Table I) net charges of La, Al, and O deviate from their formal ionic values of +3, +3, and −2, respectively. The La–O hybridization between La 5d and O 2p states lead to atomic charges of 2.43 e , 2.07 e , and −1.50 e for La, Al, and O, respectively. As a result, LaO and AlO₂ monolayers possess a bulk monolayer charge of $\pm 0.93e$ instead of formal ionic $\pm 1e$ charge. According to the Table III surface monolayer of LaO-terminated LAO(001) attracts 0.32 electrons, while other monolayers of the slab get the rest of 0.14 electrons to compensate the surface polarity. On the contrary, surface monolayer of AlO₂ terminated LAO(001) solely receives 0.46 holes. Covalency of surface La–O bond is only slightly increased (bond population increased only by 10 milli e), while calculated covalency of surface Al–O bond is practically two times larger than in the bulk, that, to some extent, may compensate relatively modest surface relaxation of AlO₂-terminated LAO(001) with respect to LaO-terminated one (see Table II).

Fig. 1 shows the density of states (DOS) projected onto all orbitals of La, Al, and O atoms of LAO bulk and both LaO- and AlO₂-terminated LAO(001) surfaces as well. In case of LAO bulk (Fig. 1c) the top of valence band is formed by O 2p orbitals, while the bottom of conduction band is formed mainly by La 5d states. La–O hybridization is well pronounced. Calculated band gap of 5.51 eV is in excellent agreement with its experimental value of 5.6 eV.³⁸ In case of LaO-terminated surface (Fig. 1a) gained excess of electrons shifts the Fermi level up to unoccupied level that gives raise to electron conductivity. In its turn the AlO₂-terminated surface (Fig. 1b) experiences the lack of electrons that shifts Fermi level down to valence band and thus reveals the existence of hole conductivity.

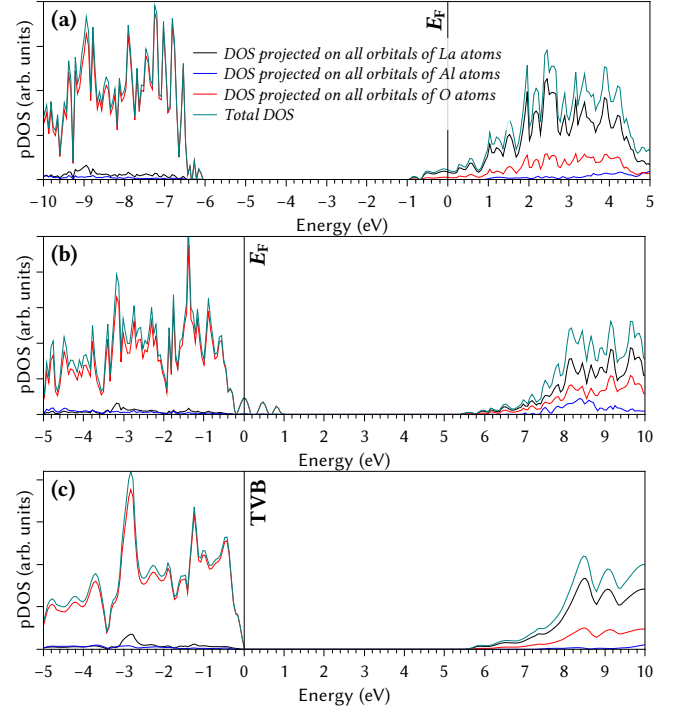


FIG. 1: (Color online) Projected density of states as calculated by means of B3PW hybrid exchange–correlation functional: (a) LaO-terminated LAO(001), (b) AlO₂-terminated LAO(001), (c) LAO bulk.

2. Thermodynamic stability

The thermodynamic formalism adopted in the current study to estimate the stability of both LaO- and AlO₂-terminated LAO(001) surfaces has been thoroughly described in Refs.45 and 46 (see also references therein). The stable crystalline surface has to be in equilibrium with both LAO bulk and surrounding oxygen atmosphere assuming that an exchange of atoms between surface and environment is allowed. Therefore, the most stable surface has the lowest Gibbs free surface energy defined as

$$\Omega_t(T, p) = \frac{1}{2A} [E_t^{slab} - N_{Al} E_{bulk}^{LAO} - (N_{La} - N_{Al}) \Delta\mu_{La} - (N_O - 3N_{Al}) \Delta\mu_O(T, p)], \quad (2)$$

where t indicates the surface terminations, A the unit cell surface area, N_i the number of atoms of type i in the slab unit cell, E_t^{slab} is the total energy of a slab with t surface terminations and E_{bulk}^{LAO} is the LAO total energy averaged per five-atom perovskite unit cell. $\Delta\mu_i = \mu_i - E_{bulk}^i$, ($i = La, Al$) are deviations of chemical potentials for metal atoms from their energy in the bulk metals. For the oxygen atom such a deviation is considered with respect to the energy of an oxygen atom in the ground triplet state of an O₂ molecule $\Delta\mu_O = \mu_O - \frac{1}{2} E^{O_2}$. Because pV term (V is unit cell volume) and the differences in vibrational Gibbs free energy between the bulk solid and a corresponding slab is negligibly small,⁴⁷ we

TABLE IV: Formation energies per formula unit used in analysis of surface stability. Experimental values are taken from Ref.48.

Material	E^f , eV	Exp. E^f , eV
La ₂ O ₃	-17.52	-18.64
Al ₂ O ₃	-16.68	-17.37
LaAlO ₃	-17.68	

omit these two contributions. This permits replacing the Gibbs free energies in Eq. (2) and in the following formulæ with the total energies obtained from *ab initio* calculations.

In order to avoid the precipitation of relevant metals and oxides at LAO surface, as well as to prevent metal atoms to leave the sample the following conditions must be satisfied:

$$0 > \Delta\mu_{\text{La}}, \quad 0 > \Delta\mu_{\text{Al}}, \quad (3)$$

$$E_{\text{LaAlO}_3}^f - E_{\text{Al}_2\text{O}_3}^f < 2\Delta\mu_{\text{La}} + 3\Delta\mu_{\text{O}} < E_{\text{La}_2\text{O}_3}^f, \quad (4)$$

where E_n^f is the formation energies of material n listed in Table IV.

We evaluate the oxygen chemical potential $\Delta\mu_{\text{O}}(p, T)$ as a function of partial gas pressure and temperature using the standard experimental thermodynamical tables⁴⁸ as it was done in Refs.46,47. $\Delta\mu_{\text{O}}(T, p_{\text{O}_2})$ is the variation of oxygen chemical potential due to temperature and pressure of the surrounding oxygen atmosphere. In addition to the experimental variation it contains a correction term $\delta\mu_{\text{O}}^0 = 0.03$ eV, which compensates the difference between the experimentally determined variation of the oxygen chemical potential and the reference state in current theoretical calculations (see Refs.49 and50 for a thorough discussion).

Based on Eqs. 2, 3, and 4, the thermodynamic stability diagram is plotted in Figs. 2, showing the regions of stability of pristine LAO(001) surfaces with respect to precipitation of La₂O₃ and Al₂O₃ oxides. Fig. 3 shows the thermodynamic stability diagram along the lines corresponding to precipitation of La₂O₃ and Al₂O₃ oxides as a function of $\Delta\mu_{\text{O}}$ related to the temperature scale at an oxygen pressure typical during LAO/STO synthesis ($P = 10^{-6}$ mbar). To make such a diagram possible, according to prescription given in Ref.51 we replaced $\Delta\mu_{\text{La}}$ by

$$\Delta\mu_{\text{La}} = \frac{1}{2}(E_{\text{La}_2\text{O}_3}^f - 3\Delta\mu_{\text{O}}), \quad (5)$$

that corresponds to precipitation of La₂O₃ (lines 3 in Fig. 3) and by

$$\Delta\mu_{\text{La}} = E_{\text{LaAlO}_3}^f - \frac{1}{2}(E_{\text{Al}_2\text{O}_3}^f - \frac{3}{2}\Delta\mu_{\text{O}}), \quad (6)$$

that corresponds to precipitation of Al₂O₃ (lines 4 in Fig. 3). Formation energies for oxides are taken from the Table IV.

From the calculated thermodynamic stability diagrams we can predict that at ultra-high vacuum (UHV) conditions typical during PLD synthesis of LAO/STO interfaces and low temperatures ($T < 550$ K) the most stable is AlO₂-terminated surface, while at elevated temperatures ($T > 1100$ K) stabilizes LaO-terminated surface. Between these temperatures both surface terminations may coexist. Further lowering of oxygen pressure shifts down these demarcated temperatures. This our prediction is in good qualitative agreement with time-of-flight scattering and recoiling spectrometry (TOF-SARS), atomic force microscopy (AFM), and photoelectron spectroscopy (PES) study performed by Rabalais and co-workers.^{52,53} They found that at temperatures less than 423 K, the surface is exclusively terminated by an Al-O layer, while at temperatures above 523 K the surface is exclusively terminated by a La-O layer. Between 423 K and 523 K surface stoichiometry changed from AlO_x to LaO_x and thus mixed terminations were proposed. Moreover this change was found to be fully reversible. Rabalais and co-workers suggested that the surface termination change was caused by the formation of surface oxygen vacancies at high temperature, which drives the migration of the La atom to the surface and the Al atom into the bulk. More recent experimental study based on X-ray crystal truncation rod (CRT) analysis⁵⁴ demonstrates that LAO(001) possesses Al-terminated structure at both room and high (670 K) temperatures with no evidence for the reversal of surface termination or for the formation of surface oxygen vacancy. Authors of Ref.54 explain the observation of La-rich termination in ion-scattering experiments^{52,53} by the effect of the increasing access to the lanthanum atom because of considerable surface oxygen relaxation that leads to a significant enhancement of the lanthanum atom signature. On the other hand, Marx and co-workers have observed the La-terminated LAO(001) with stoichiometry of $(\text{VLa}_4\text{O}_5)^{-0.5}$, where V is the lanthanum cation vacancy, i.e., each surface La is coordinate to four surface oxygens and four oxygens in the subsurface layer.⁵⁵ Therefore one may conclude that the experimental analyses have been performed at various conditions and report either LaO- and AlO₂-terminated LAO(001) or mixture of them, so it is not clear if surfaces reached thermodynamic equilibrium or not.

Ab initio thermodynamical stability diagrams previously calculated for LAO(001) shows that LaO-terminated surface is more stable with respect to AlO₂-terminated one⁴³ and LaO-terminated surface containing oxygen vacancy is more stable than oxygen deficient AlO₂-terminated LAO(001) as well.⁴² Mixed surfaces with LaO- and AlO₂-terminations were not predicted. In fact, our thermodynamic analysis does not support this prediction.

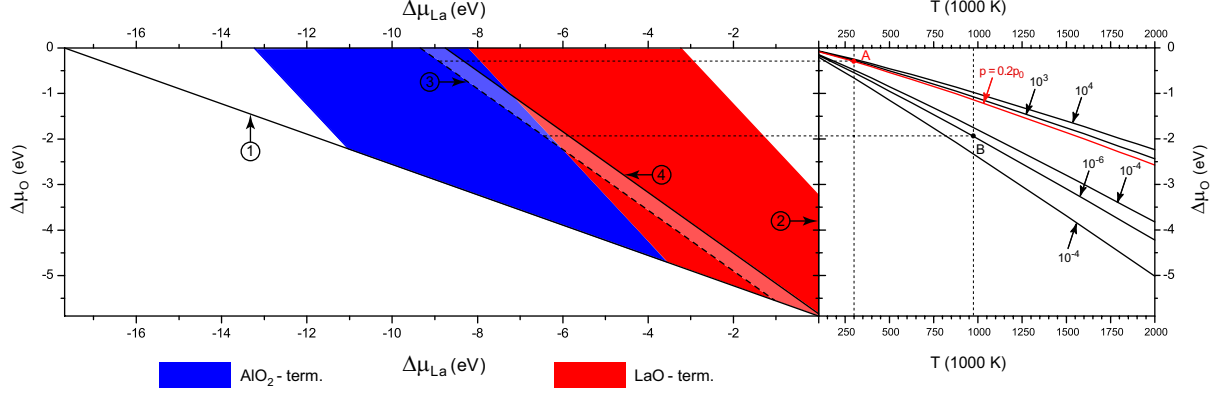


FIG. 2: (Color online) Thermodynamic stability diagram as a function of O and La chemical potentials built for both LaO- and AlO_2 -terminated LAO(001) surfaces. Diagram contains precipitation conditions for both La and Mn metals, as well as for their trivalent oxides (La_2O_3 and Al_2O_3). Stable region is shown as shaded area between La_2O_3 and Al_2O_3 precipitation lines. The numbers from 1 to 4 in the circles indicate segregation lines for precipitation of: 1. Al, 2. La, 3. La_2O_3 , 4. Al_2O_3 . The right side shows a family of oxygen chemical potentials under different conditions. The label m indicates the O_2 gas partial pressure: 10^m mbar. Red (gray) line corresponds to oxygen partial pressure $p = 0.2p_0$ as in the ambient atmosphere. Point A stands for room temperature and ambient oxygen pressure, point B stands for typical temperature and pressure during LAO/STO(001) synthesis.

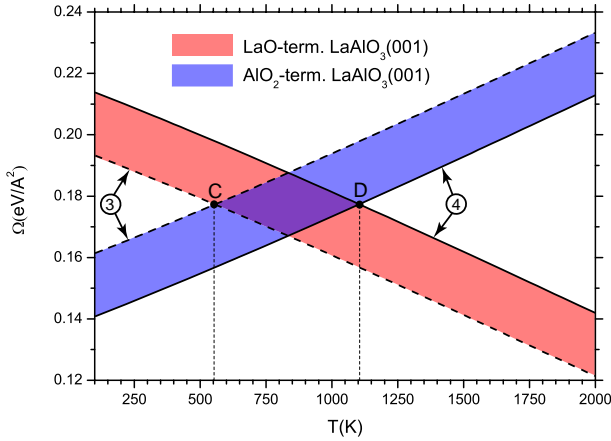


FIG. 3: (Color online) The thermodynamic stability diagram calculated along the La_2O_3 and Al_2O_3 precipitation lines (number 3 and 4 in the circles, respectively) with $\Delta\mu_{\text{La}}$ defined according to Eqs. 5 and 6. The dependence on the oxygen chemical potential is converted to the appropriate temperature scale at an oxygen pressure typical during LAO/STO(001) synthesis ($P = 10^{-6}$ mbar). The interval between points C and D correspond to temperature range where both LaO- and AlO_2 -terminated LAO(001) surfaces are stable and may coexist.

B. LAO/STO heterointerfaces

1. Atomic structure

Calculations of geometric and electronic properties of the LAO/STO(001) heterointerfaces were carried out using the symmetrically terminated slab model. The STO(001) substrate consisted of 11 atomic monolayers

and could be terminated with either $(\text{TiO})_2^0$ monolayer in n-type heterostructures or with $(\text{SrO})^0$ monolayer in p-type heterostructures. Then monolayer-by-monolayer epitaxial growth is modeled adding a pair of respective monolayers of LAO(001) symmetrically to both sides of a substrate slab until deposited LAO(001) thin film reach thickness of up to 11 monolayers. In such a way we construct 22 heterostructures of both types and of different LAO film thickness to model.

Due to the restrictions by imposed symmetry, in our calculations atomic positions of all the heterointerfaces under study were relaxed along the z axis. Displacements Δz were calculated with respect to the averaged position z of the previous atomic monolayer as defined in Eq. (1) to avoid constant increase in the value of the former. These computations were held for results, obtained using both CRYSTAL and VASP and are summarized in Fig. 4a–d for n- and p-type LAO/STO(001) heterointerfaces.

From these figures one can see that the displacements obtained by means of LCAO and PW approaches are in a good agreement. All the shifts are within 10% of the lattice constant. The STO(001) substrate contracts on the average with respect to the bulk phase, while the LAO(001) thin film, on the contrary, expands to compensate the lattice mismatch.

For n-type stoichiometric interfaces containing 10 LAO monolayers (Fig. 4a), in good agreement with recent theoretical study performed by Yang and Su (Ref.56), our calculations predict that all the atoms in the substrate relax slightly (by 0.04 Å) towards the LAO film. La atoms of the inner monolayers are displaced towards the surface by 0.16 Å, whereas Al atoms are displaced towards the interface by 0.06 Å. Oxygen atoms relaxed towards the interface by 0.06 Å in LaO monolayers and by 0.20 Å in AlO_2 monolayers. The La atom of the top-most mono-

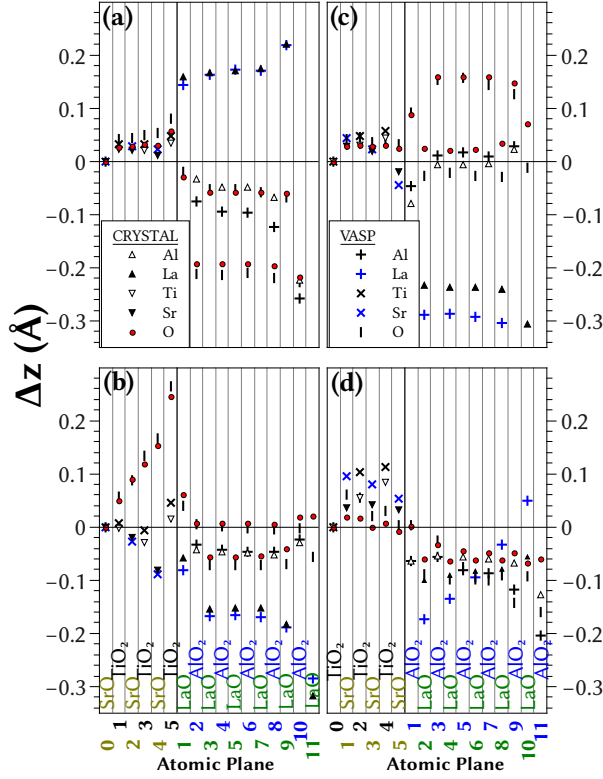


FIG. 4: (Color online) calculated atomic displacements along z -axis for (a, b) n-LAO/STO(001) and (c, d) p-LAO/STO(001) heterostructures. Reference z -coordinate for each monolayer is defined so that it includes the displacement of preceding atomic monolayer (see Eq. 1). Both LCAO-B3PW (CRYSTAL) and PW-PW91 (VASP) results are present. The x axis shows the atomic monolayers from which atoms are originated. STO and LAO monolayers are numbered beginning from the center of slab (0 means the central monolayer of the symmetrical slab unit cell). Monolayers are numbered separately for STO(001) substrate and for LAO(001) nanofilm. Panels (a, c) show atomic displacements for $N_{\text{LAO}} = 10$, while panels (b, d) – for $N_{\text{LAO}} = 11$.

layer is displaced by 0.20 \AA and the relaxation of Al atom in the penultimate monolayer is also somewhat greater (0.22 \AA) than in the others.

In p-type LAO/STO(001) with 10 monolayers of LAO (Fig. 4c) only positions of oxygen atoms of AlO_2 monolayers and La atoms of LaO monolayers have substantially changed by 0.16 \AA and -0.24 \AA , respectively for inner monolayers. The atoms of the top-most monolayer again show deviation from the tendencies and its La atom has shifted even more to the interface (-0.30 \AA), but O atom has relaxed less (by 0.08 \AA).

In non-stoichiometric n-type interfaces (Fig. 4b) the substrate is distorted: Its O atoms are shifted towards the interface, whereas cations are shifted in the opposite direction. The shift dependance on the layer number is linear. Cations of the LAO film are shifted towards the interface: La by 0.16 \AA and Al by 0.04 \AA . Oxygen

atoms of LaO monolayers shift in the same direction by 0.04 \AA , while oxygens from AlO_2 monolayers do not shift at all. The La atom of the top-most layer doubles normal displacement and is shifted by -0.32 \AA , while the oxygen atom of the same monolayer shifts weakly towards the surface.

Non-stoichiometric p-type interfaces (Figure 4d) show no relaxation for the O atoms of the substrate, whereas cations thereof are shifted no more than by 0.1 \AA towards the interface. Atoms of the LAO film are also shifted towards the interface plane by ca. 0.5 \AA . The shift of Al atoms of the top-most layer is approximately twice as large, as in the inner layers – ca. 0.1 \AA .

Another important observation is that cations and anions in LAO monolayers have considerably different displacements, thus electric dipole moment appears and accumulates within the thin film. It is worth noting that stoichiometric heterointerfaces have greater displacement differences between anions and cations than non-stoichiometric ones in LAO monolayers, while the situation is diametrically opposite for the STO monolayers. As we shall see further, the dipole moment creates an electric field, whose potential strongly correlates with the distortion of the band edges (so-called polar distortion), which then gives rise to the conductivity in stoichiometric LAO/STO(001) heterointerfaces of n-type.

Tendencies in the atomic shifts are preserved in the thinner structures and may be seen in the respective graphs in the Supplementary Materials.

2. Charge redistribution and electronic properties

To predict the charge redistribution in heterointerfaces we calculated the changes of net atomic Mulliken charges in comparison with the bulk phase of the LAO and STO parent materials. These charge deviations are shown in Fig. 5a–d for LAO/STO(001) heterointerfaces of n- and p-type. From these one can clearly see, that deviation of charges are relatively small in the inner monolayers of the LAO film in n-type LAO/STO(001), not exceeding $0.03e$, whereas the same layers in the p-type LAO/STO(001) show quite large charge deviations $\pm 0.35 \div 0.40e$ from the parent bulk, and these are negative for AlO_2 monolayers and positive for LaO monolayers.

In both n- and p-type interfaces charges on the substrate monolayers did not vary substantially. For stoichiometric n-type and non-stoichiometric p-type interfaces these are about $\pm 0.04e$ for TiO_2 and SrO , respectively. On the other hand, stoichiometric p-type interfaces show a small positive deviation of TiO_2 monolayer charges (ca. $0.01e$) and about ten times bigger negative charge deviation for SrO monolayers. Charge shifts in the substrates of stoichiometric n-type structures are all negative, and SrO shifts (ca. $0.04e$) are smaller than TiO_2 shifts of ca. $0.06e$.

Most significant deviations in atomic charges of n-type structures are located in the top-most monolayer –

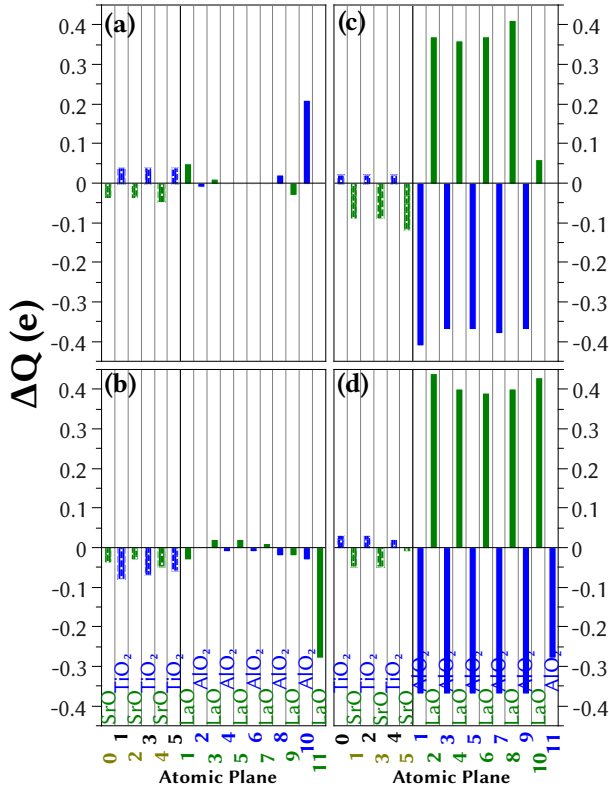


FIG. 5: (Color online) Calculated deviations of Mulliken effective charge densities (ΔP_Q) in AO- and BO_2 -monolayers of (a, b) n-LAO/STO(001) and (c, d) p-LAO/STO(001) heterostructures with respect to charge densities in AO- and BO_2 -monolayers of STO and LAO bulk, correspondingly. Calculations are performed using B3PW hybrid exchange-correlation functional. The x axis shows the atomic monolayers from which atoms are originated. STO and LAO monolayers are numbered starting from the center of slab (0 means the central monolayer of the symmetrical slab unit cell). Monolayers (planes) are numbered separately for STO(001) substrate and for LAO(001) nanofilm. Panels (a, c) show charge density deviation for $N_{\text{LAO}} = 10$, while panels (b, d) – for $N_{\text{LAO}} = 11$.

$+0.2e$ for stoichiometric structures and $-0.25e$ for non-stoichiometric ones – due to the surface effects and thus compensate the “polar catastrophe” as proposed from a pure ionic model.⁹ In p-type structures charge shifts in the surface layers are less pronounced than in the inner layers of the film and are $+0.05e$ and $-0.27e$ for LaO- and AlO_2 -terminated structures, respectively.

Here charge redistribution only in the thickest structures investigated is shown. Respective graphs for thinner structures can be found in Supplementary Materials.

Another way to look at the problem of charge redistribution is to calculate, what happens with the electronic charge density in the heterostructures, compared to the isolated LAO and STO slab parts. Charge density redistribution is defined as the electronic density in the heterointerface minus the sum of electron densities in separately isolated STO(001) substrate and LAO(001) thin

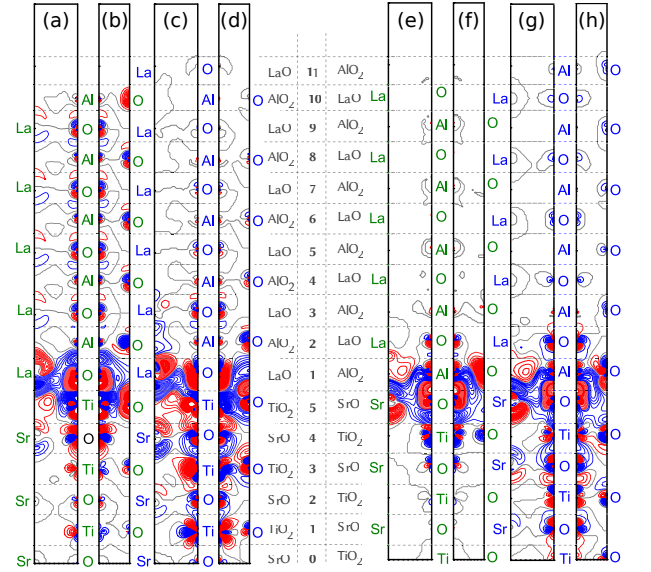


FIG. 6: (Color online) Difference electron charge density maps calculated for (a-d) n-LAO/STO(001) and (e-h) p-LAO/STO(001) heterostructures: (a, e) (110) cross-section for $N_{\text{LAO}} = 10$, (b, f) (100) cross-section for $N_{\text{LAO}} = 10$, (c, g) (110) cross-section for $N_{\text{LAO}} = 11$, (d, h) (100) cross-section for $N_{\text{LAO}} = 11$. Red (dark gray), blue (light gray) and gray isolines describe positive, negative and zero values of the difference charge density, respectively. Isodensity curves are drawn from -0.025 to $+0.025 e \text{ \AA}^{-3}$ with an increment of $0.0005 e \text{ \AA}^{-3}$. Right-side bar shows the atomic monolayers from which atoms are originated. Calculations are performed using B3PW hybrid exchange-correlation functional. STO and LAO monolayers are numbered beginning from the center of slab (0 means the central monolayer of the symmetrical slab unit cell). Monolayers (planes) are numbered separately for STO(001) substrate and for LAO(001) nanofilm.

film slabs and is depicted in Fig. 6 for both n- and p-type LAO/STO(001) interfaces.

These plots show us that the most significant distortions occur at the interface due to the compensation of the surface effects of the slabs. They also show that the electronic structure of the substrate of non-stoichiometric heterostructures is distorted stronger than that of stoichiometric ones. The situation in the thin films is opposite. This fact correlates with the argument in the section on atomic structure.

More illustrative property to consider is the polarization of all four of stoichiometric and non-stoichiometric n- and p-type heterointerfaces, which was already briefly introduced. It allows us to explain certain phenomena, such as the polar distortion, as well as to provide a mechanism for a partial compensation of the “polar catastrophe”.

Each one of considered interfaces possesses no net charge, thus it can be divided into multiple neutral slabs normal to z , in which net charge is also zero and so average polarization of such slabs can be calculated. The charge density function, which should be used in the cal-

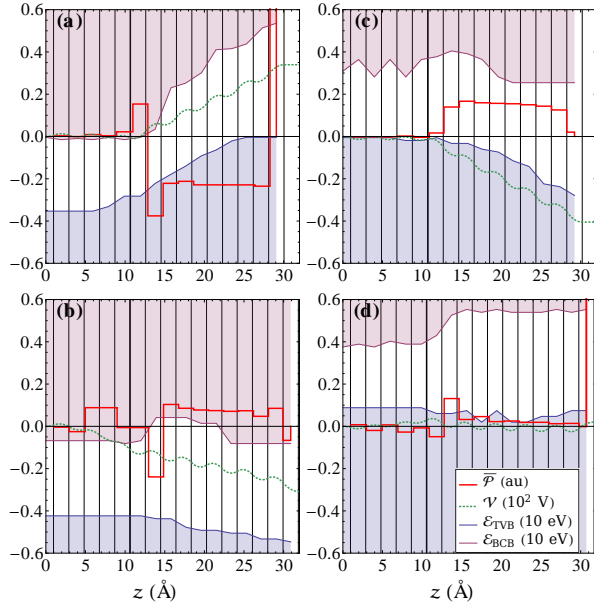


FIG. 7: (Color online) Polarization (as calculated using Eq. (7)), band edges and electrostatic potential of (a, b) n-LAO/STO(001) and (c, d) p-LAO/STO(001) heterostructures with (a, c) $N_{\text{LAO}} = 10$ and (b, d) $N_{\text{LAO}} = 11$ LAO monolayers. Zero at the energy scale corresponds to the Fermi level. Distances are measured from the central monolayer of the symmetrical slab unit cell.

culations, is estimated as if the charge of each atom A is uniformly distributed over the plane $z = z_A$, reducing the task to one dimension. Thus the projection of polarization vector on z -axis can be calculated as

$$\bar{P}_i = \frac{\sum_A z_A Q_A}{\Delta z}, \quad (7)$$

Q_A is the charge on atom A, Δz is the thickness of the electroneutral allocated slab, to which the atom A belongs and summation is performed over all the atoms in the i -th neutral slab.

In order to divide the interface in neutral slabs, it sometimes is necessary to split one monolayer's charge: One part of it compensates the remaining charge of the previous slab and the remainder goes to the next one.

The resulting polarization function $\bar{P}(z)$ is averaged using the moving average function, and the results for n- and p-type interfaces are shown together with the energies of band boundaries E_{TVB} and E_{BCB} and the potential due to intrinsic electrostatic field V in Fig. 7. Here one can see, that LAO films of stoichiometric interfaces are strongly polarized, giving rise to the polar distortion of band edges. On the other hand, there is rather a weak LAO polarization in the non-stoichiometric interfaces meaning a weak polar distortion as is observed. The substrate is polarized more in non-stoichiometric case, which corresponds to Figs. 6c,d and Figs. 6g,h.

In each of the structures there is a substantial polarization in the top-most monolayer, which is correlated with

TABLE V: Band gaps (δ in eV) or sheet carrier density (n_s in 10^{14} cm^{-2}) of n-LAO/STO heterointerfaces as calculated by means of hybrid B3PW and PW91 exchange-correlation functionals. $N_{\text{tot}}^{\text{LAO}}$ stands for the total number of LAO(001) monolayers deposited atop STO(001) substrate.

$N_{\text{tot}}^{\text{LAO}}$	Term. m-layer	B3PW (CRYSTAL)		PW91 (VASP)	
		δ	n_s	δ	n_s
1	LaO	—	6.04	—	—
2	AlO ₂	3.65	—	1.41	—
3	LaO	—	6.07	—	—
4	AlO ₂	2.91	—	1.03	—
5	LaO	—	5.91	—	—
6	AlO ₂	1.96	—	0.40	—
7	LaO	—	6.20	—	—
8	AlO ₂	1.07	—	0.03	—
9	LaO	—	6.27	—	—
10	AlO ₂	—	1.56	—	0.16
11	LaO	—	6.13	—	0.54

TABLE VI: The same as Table V, but for p-LAO/STO(001) heterostructures.

$N_{\text{tot}}^{\text{LAO}}$	Term. m-layer	B3PW (CRYSTAL)		PW91 (VASP)	
		δ	n_s	δ	n_s
1	AlO ₂	—	6.65	—	—
2	LaO	4.00	—	1.60	—
3	AlO ₂	—	7.27	—	—
4	LaO	4.05	—	1.69	—
5	AlO ₂	—	9.08	—	—
6	LaO	4.05	—	1.51	—
7	AlO ₂	—	7.90	—	—
8	LaO	3.80	—	0.48	—
9	AlO ₂	—	6.97	—	—
10	LaO	2.92	—	0.25	—
11	AlO ₂	—	10.2	—	0.12

the excessive charge density there and, for stoichiometric interfaces, with the “polar catastrophe” compensation mechanism. The interface monolayers are also polarized.

Electronic properties in a more experimentally measurable way can be represented as band gaps for insulating structures or as the concentration of charge carriers for conductors. These data obtained with CRYSTAL and VASP are represented in Tables V and VI for n- and p-type structures, respectively. Firstly, one can see that all the non-stoichiometric interfaces are conducting and free charge concentration is roughly equal within a type and does not depend on the LAO film thickness. p-Type structures possess greater carrier density than n-type structures, though experiments never showed conductive behavior in the former.

For stoichiometric structures insulating behavior is the default one. The thickness of the band gap decreases with the thickness of the LAO film both for n- and p-type structures. This eventually leads to the closing of the gap for the n-type interfaces with $N_{\text{LAO}} \geq 10$ monolayers, which is in a good accordance with experimental works.

The gap-diminishing tendency is less pronounced for the p-type structures and thus they are not found conducting at any thickness within this study.

The results obtained with VASP are given for qualitative comparison. They showed out to be in accordance with CRYSTAL results, but due to the specifics of the non-hybrid functional band gaps and free charge concentrations are far too small. CRYSTAL, on the other hand, gives plausible results comparing to experimental data.

The total band gap described above gives us some valuable data on conducting–insulating behavior of the interfaces of different types. Nevertheless, it does not give us much information about the origin of conductivity. Thus it is more worthy to look at the positions of the band edges in energy scale separately for each monolayer. Such a decomposition is depicted in aforementioned Figures 7a,b and 7c,d for n- and p-type structures, respectively. From these plots one can see, that band edges for stoichiometric interfaces are distorted, besides such a distortion leads to n-type conductivity in n-type structures thick enough and might hypothetically lead to the p-type conductivity in thicker p-type structures than investigated. Non-stoichiometric interfaces show little or no polar distortion, but it is not necessary for the appearance of the conductivity, because such structures contain non-stoichiometric LAO films, which are already conducting on their own. Our prediction on conductivity of non-stoichiometric LaO-terminated n-type LAO/STO(001) interface is in agreement with a recent theoretical study performed by Pavlenko and Kopp (See Ref.57) in which they show that LaO-terminated n-type LAO/STO(001) interface is metallic.

IV. SUMMARY AND CONCLUDING REMARKS

We have performed large-scale first-principles calculations on a number of both stoichiometric and non-

stoichiometric LAO/STO(001) heterostructures. Two different *ab initio* approaches have been applied: LCAO with hybrid B3PW and PW with PW91 exchange–correlation functionals within DFT. Consistently within both approaches we predict that there exists a distortion in energies of band edges for stoichiometric structures which eventually leads to the appearance of the conductivity at a critical thickness in n-type interfaces or to the reduction of the band gap for p-type interfaces. Non-stoichiometric interfaces were found to be conducting independently of the LAO film thickness and possessing little or no distortion of band edges. The conductivity appears due to the non-stoichiometry of the thin film which is a conductor on its own, as we demonstrate by a separate analysis of an isolated film.

The degree of distortion of the band edges agree well with the estimates of the internal electric field generated by changes in the atomic charges and the geometric relaxation of the atomic structure. We confirm these factors as the ones responsible for the rise of conductivity in stoichiometric n-type heterostructures. Calculated concentration of the free charge in the interfaces roughly agrees with the experimental data, being somewhat underestimated.

Acknowledgments

This work has been supported through the ESF project Nr.2009/0216/1DP/1.1.1.2.0/09/APIA/VIAA/044. The authors are thankful to R. Evarestov, A. Shluger, E. Kotoomin, Yu. Purans, E. Heifets, Yu. Zhukovskii, J. Timoshenko and P. Nazarov for stimulating discussions.

* Electronic address: as08504@lu.lv

¹ A. Ohtomo and H. Y. Hwang, *Nature* **427**, 423 (2004).

² H. Y. Hwang, Y. Iwasa, M. Kawasaki, B. Keimer, N. Nagaosa, and Y. Tokura, *Nat. Mater.* **11**, 103 (2012).

³ H. Chen, A. M. Kolpak, and S. Ismail-Beigi, *Adv. Mater.* **22**, 2881 (2010).

⁴ R. Pentcheva and W. E. Pickett, *J. Phys.: Cond. Matter* **22**, 043001 (2010).

⁵ S. Chambers, M. Engelhard, V. Shutthanandan, Z. Zhu, T. Droubay, L. Qiao, P. Sushko, T. Feng, H. Lee, T. Gustafsson, E. Garfunkel, A. Shah, J.-M. Zuo, and Q. Ramasse, *Surf. Sci. Rep.* **65**, 317 (2010).

⁶ R. Jany, M. Breitschaft, G. Hammerl, A. Horsche, C. Richter, S. Paetel, J. Mannhart, N. Stucki, N. Reyren, S. Gariglio, P. Zubko, A. D. Caviglia, and J.-M. Triscone, *Appl. Phys. Lett.* **96**, 183504 (2010).

⁷ C. Cen, S. Thiel, G. Hammerl, C. W. Schneider, K. E. An-

dersen, C. S. Hellberg, J. Mannhart, and J. Levy, *Nature Mat.* **7**, 298 (2008).

⁸ B. Forgy, C. Richter, and J. Mannhart, *Appl. Phys. Lett.* **100**, 053506 (2012).

⁹ N. Nakagawa, H. Y. Hwang, and D. A. Muller, *Nature Mat.* **5**, 204 (2006).

¹⁰ Y. Segal, J. H. Ngai, J. W. Reiner, F. J. Walker, and C. H. Ahn, *Phys. Rev. B* **80**, 241107 (2009).

¹¹ W.-j. Son, E. Cho, B. Lee, J. Lee, and S. Han, *Phys. Rev. B* **79**, 245411 (2009).

¹² H. Chen, A. Kolpak, and S. Ismail-Beigi, *Phys. Rev. B* **82**, 085430 (2010).

¹³ Y. Li and J. Yu, *J. Appl. Phys.* **108**, 013701 (2010).

¹⁴ M. Basletic, J. Maurice, C. Carrétéro, G. Herranz, O. Copie, M. Bibes, É. Jaquet, K. Bouzehouane, S. Fusil, and A. Barthélémy, *Nature Mat.* **7**, 621 (2008).

¹⁵ H. Chen, A. M. Kolpak, and S. Ismail-Beigi, *Phys. Rev.*

- B **79**, 161402 (2009).
- ¹⁶ A. S. Kalabukhov, Y. A. Boikov, I. T. Serenkov, V. I. Sakharov, V. N. Popok, R. Gunnarsson, J. Börjesson, N. Ljustina, E. Olsson, D. Winkler, and T. Claeson, *Phys. Rev. Lett.* **103**, 146101 (2009).
 - ¹⁷ A. Kalabukhov, Y. A. Boikov, I. T. Serenkov, V. I. Sakharov, J. Börjesson, N. Ljustina, E. Olsson, D. Winkler, and T. Claeson, *EPL* **93**, 37001 (2011).
 - ¹⁸ L. Qiao, T. C. Droubay, V. Shutthanandan, Z. Zhu, P. V. Sushko, and S. A. Chambers, *J. Phys.: Cond. Matter* **22**, 312201 (2010).
 - ¹⁹ L. Qiao, T. C. Droubay, T. Varga, M. E. Bowden, V. Shutthanandan, Z. Zhu, T. C. Kaspar, and S. A. Chambers, *Phys. Rev. B* **83**, 085408 (2011).
 - ²⁰ T. C. Droubay, L. Qiao, T. C. Kaspar, M. H. Engelhard, V. Shutthanandan, and S. A. Chambers, *Appl. Phys. Lett.* **97**, 124105 (2010).
 - ²¹ A. D. Becke, *J. Chem. Phys.* **98**, 5648 (1993).
 - ²² R. Dovesi, V. R. Saunders, C. Roetti, R. Orlando, C. M. Zicovich-Wilson, F. Pascale, B. Civalleri, K. Doll, N. M. Harrison, I. J. Bush, Ph. D'Arco, and M. Llunell, *CRYSTAL09 User's Manual*, University of Torino, Torino (2009), <http://www.crystal.unito.it/>.
 - ²³ J. P. Perdew and Y. Wang, *Phys. Rev. B* **33**, 8800 (1986).
 - ²⁴ J. P. Perdew and Y. Wang, *Phys. Rev. B* **45**, 13244 (1992).
 - ²⁵ G. Kresse, M. Marsman, and J. Furthmüller, *VASP the GUIDE*, University of Wien, Wien (2011), <http://cms.mpi.univie.ac.at/VASP/>.
 - ²⁶ S. Piskunov, E. Heifets, R. I. Eglitis, and G. Borstel, *Comp. Mat. Sci.* **29**, 165 (2004).
 - ²⁷ Y. F. Zhukovskii, N. Pugno, A. I. Popov, C. Balasubramanian, and S. Bellucci, *J. Phys.: Cond. Matt.* **19**, 395021 (2007).
 - ²⁸ S. Piskunov, E. Spohr, T. Jacob, E. A. Kotomin, and D. E. Ellis, *Phys. Rev. B* **76**, 012410 (2007).
 - ²⁹ P. J. Hay and W. R. Wadt, *J. Chem. Phys.* **82**, 299 (1984).
 - ³⁰ M. Dolg, H. Stoll, A. Savin, and H. Preuss, *Theor. Chim. Acta* **75**, 173 (1989).
 - ³¹ S. Piskunov, A. Gopeyenko, E. A. Kotomin, Y. F. Zhukovskii, and D. E. Ellis, *Comput. Mater. Sci.* **41**, 195 (2007).
 - ³² S. Piskunov, E. A. Kotomin, E. Heifets, J. Maier, R. I. Eglitis, and G. Borstel, *Surf. Sci.* **575**, 75 (2005).
 - ³³ E. A. Kotomin, S. Piskunov, Y. F. Zhukovskii, R. I. Eglitis, A. Gopeyenko, and D. E. Ellis, *Phys. Chem. Chem. Phys.* **10**, 4258 (2008).
 - ³⁴ R. F. W. Bader, *Atoms in Molecules, A Quantum Theory* (Oxford University Press, Oxford, 1990).
 - ³⁵ H. J. Monkhorst and J. D. Pack, *Phys. Rev. B* **13**, 5188 (1976).
 - ³⁶ S. A. Hayward, F. D. Morrison, S. A. T. Redfern, E. K. H. Salje, J. F. Scott, K. S. Knight, S. Tarantino, A. M. Glazer, V. Shuvaeva, P. Daniel, M. Zhang, and M. A. Carpenter, *Phys. Rev. B* **72**, 054110 (2005).
 - ³⁷ Y. A. Abramov, V. G. Tsirelson, V. E. Zavodnik, S. A. Ivanov, and I. D. Brown, *Acta Cryst. B* **51**, 942 (1995).
 - ³⁸ S.-G. Lim, S. Kriventsov, T. N. Jackson, J. H. Haeni, D. G. Schlom, A. M. Balbashov, R. Uecker, P. Reiche, J. L. Freeouf, and G. Lucovsky, *J. Appl. Phys.* **91**, 4500 (2002).
 - ³⁹ K. van Benthem, C. Elsässer, and R. H. French, *J. Appl. Phys.* **90**, 6156 (2001).
 - ⁴⁰ P. W. Tasker, *J. Phys. C: Solid State Phys.* **12**, 4977 (1979).
 - ⁴¹ A. Asthagiri and D. S. Sholl, *Phys. Rev. B* **73**, 125432 (2006).
 - ⁴² T. Jin-Long, Z. Jun, Q. Wen-Feng, X. Jie, and L. Yan-Rong, *Chinese Phys. B* **17**, 655 (2008).
 - ⁴³ J.-L. Tang, J. Zhu, W.-F. Qin, J. Xiong, Y. Zhang, and Y.-R. Li, *Phys. Lett. A* **365**, 149 (2007).
 - ⁴⁴ H. Seo and A. A. Demkov, *Phys. Rev. B* **84**, 045440 (2011).
 - ⁴⁵ S. Piskunov, E. Heifets, T. Jacob, E. A. Kotomin, D. E. Ellis, and E. Spohr, *Phys. Rev. B* **78**, 121406 (2008).
 - ⁴⁶ E. Heifets, S. Piskunov, E. A. Kotomin, Y. F. Zhukovskii, and D. E. Ellis, *Phys. Rev. B* **75**, 115417 (2007).
 - ⁴⁷ K. Reuter and M. Scheffler, *Phys. Rev. B* **65**, 035406 (2001).
 - ⁴⁸ M. W. Chase, *NIST-JANAF thermochemical tables* (Am. Chem. Soc., Washington, DC, 1998).
 - ⁴⁹ P. Kaghazchi, T. Jacob, I. Ermanoski, W. Chen, and T. E. Madey, *ACS Nano* **2**, 1280 (2008).
 - ⁵⁰ Y. A. Mastrikov, R. Merkle, E. Heifets, E. A. Kotomin, and J. Maier, *J. Phys. Chem. C* **114**, 3017 (2010).
 - ⁵¹ S. Piskunov, T. Jacob, and E. Spohr, *Phys. Rev. B* **83**, 073402 (2011).
 - ⁵² J. Yao, P. B. Merrill, S. S. Perry, D. Marton, and J. W. Rabalais, *J. Chem. Phys.* **108**, 1645 (1998).
 - ⁵³ P. A. W. van der Heide and J. W. Rabalais, *Chem. Phys. Lett.* **297**, 350 (1998).
 - ⁵⁴ R. J. Francis, S. C. Moss, and A. J. Jacobson, *Phys. Rev. B* **64**, 235425 (2001).
 - ⁵⁵ C. H. Lanier, J. M. Rondinelli, B. Deng, R. Kilaas, K. R. Poeppelmeier, and L. D. Marks, *Phys. Rev. Lett.* **98**, 086102 (2007).
 - ⁵⁶ X. Yang and H. Su, *ACS Appl. Mater. Interfaces* **3**, 3819 (2011).
 - ⁵⁷ N. Pavlenko and T. Kopp, *Surf. Sci.* **605**, 1114 (2011).